

Efficiently Extracting Multi-Point Correlations of a Floquet Thermalized System

Yong-Guang Zheng,^{1,2,3,*} Wei-Yong Zhang,^{1,2,3,*} Ying-Chao Shen,^{1,2,3,*} An Luo,^{1,2,3} Ying Liu,^{1,2,3} Ming-Gen He,^{1,2,3} Hao-Ran Zhang,^{1,2,3} Wan Lin,^{1,2,3} Han-Yi Wang,^{1,2,3} Zi-Hang Zhu,^{1,2,3} Ming-Cheng Chen,^{1,2,3} Chao-Yang Lu,^{1,2,3} Supanut Thanasilp,⁴ Dimitris G. Angelakis,^{4,5} Zhen-Sheng Yuan,^{1,2,3} and Jian-Wei Pan^{1,2,3}

¹*Hefei National Research Center for Physical Sciences at the Microscale and School of Physical Sciences, University of Science and Technology of China, Hefei 230026, China*

²*CAS Center for Excellence in Quantum Information and Quantum Physics, University of Science and Technology of China, Hefei 230026, China*

³*Hefei National Laboratory, University of Science and Technology of China, Hefei 230088, China*

⁴*Centre for Quantum Technologies, National University of Singapore, 3 Science Drive 2, Singapore 117543*

⁵*School of Electrical and Computer Engineering, Technical University of Crete, Chania, Greece 73100*

(Dated: October 18, 2022)

Nonequilibrium dynamics of many-body systems is challenging for classical computing, providing opportunities for demonstrating practical quantum computational advantage with analogue quantum simulators. It is proposed to be classically intractable to sample driven thermalized many-body states of Bose-Hubbard systems, and further extract multi-point correlations for characterizing quantum phases. Here, leveraging dedicated precise manipulations and number-resolved detection through a quantum gas microscope, we implement and sample a 32-site driven Hubbard chain in the thermalized phase. Multi-point correlations of up to 14th-order extracted from experimental samples offer clear distinctions between the thermalized and many-body-localized phases. In terms of estimated computational powers, the quantum simulator is comparable to the fastest supercomputer with currently known best algorithms. Our work paves the way towards practical quantum advantage in simulating Floquet dynamics of many-body systems.

Introduction. Periodically driven systems can exhibit exotic quantum phases of matter, such as discrete time crystals [1, 2] and many-body scars [3, 4]. In the driven ergodic phases, emergent long-range interactions lead to an infinite temperature thermalization [5–8] and a chaotic spreading throughout the entire Hilbert space. Rapid increasing entanglement during the evolution hinders efficient classical simulations of these dynamics with the currently known algorithms [9, 10], and in turn impedes extracting multi-point correlations to characterize the quantum many-body system [11].

Quantum computation is expected to prevail over its classical counterpart in simulating highly entangled quantum systems [12, 13]. Due to the frailty of the qubits and the heavy overhead in the number of qubits and number of gates required to perform error correction, much effort is still needed to successfully construct and harness the power of fault-tolerant digital universal quantum computers [10, 14, 15]. On the other hand, the rapid development of analogue quantum simulators makes it a promising alternative for practical applications of near-term quantum hardware [16, 17]. Analogue simulators with the inherent many-body nature directly mimic the problems of interest in condensed matter and high-energy physics, and in general, are more hardware-friendly than digital ones, as they require much less local controls and the extra layer of translation into gates is not necessary [10, 14].

Notably, the computational task of sampling from a periodically driven thermalized many-body system has been proposed to demonstrate practical quantum computational advantage backed by complexity-theoretic foundations [8, 18], which also provides identifications of dynamical phases in the driven system through multi-point density correlations simultaneously. For low-frequency driving and low disorders, the system will thermalize and the associated temperature becomes infinite. In this limit, the Floquet operator U_F is intimately related to a random matrix drawn from the circular orthogonal ensemble (COE), where sampling the probability distribution of the final state is classically intractable [8, 18]. In contrast, classical simulation is feasible in the many-body-localized (MBL) phase due to an area-law scaling of entanglement. Therefore, sampling the many-body system and extracted multi-point correlations from the samples while varying the parameters will give information on the dynamical phase diagram, which is beyond the characterizations of the quantum machine itself [19–24].

In the present work, we implement a driven Bose-Hubbard model in optical lattices and draw samples from the output probability distribution encoded in the states of the thermalized phase in a 32-site chain with 20 particles, which is a classically intractable regime. Site-resolved manipulations enable deterministic initialisation and periodically driving of the system. The stability of the set-up and precise calibrations offer us the ability for quantitatively reliable quantum simulation of the many-body dynamics. After the final state is projected on a Fock basis, we utilise the atom-number readout to obtain the output strings. For

* These authors contributed equally to this work.

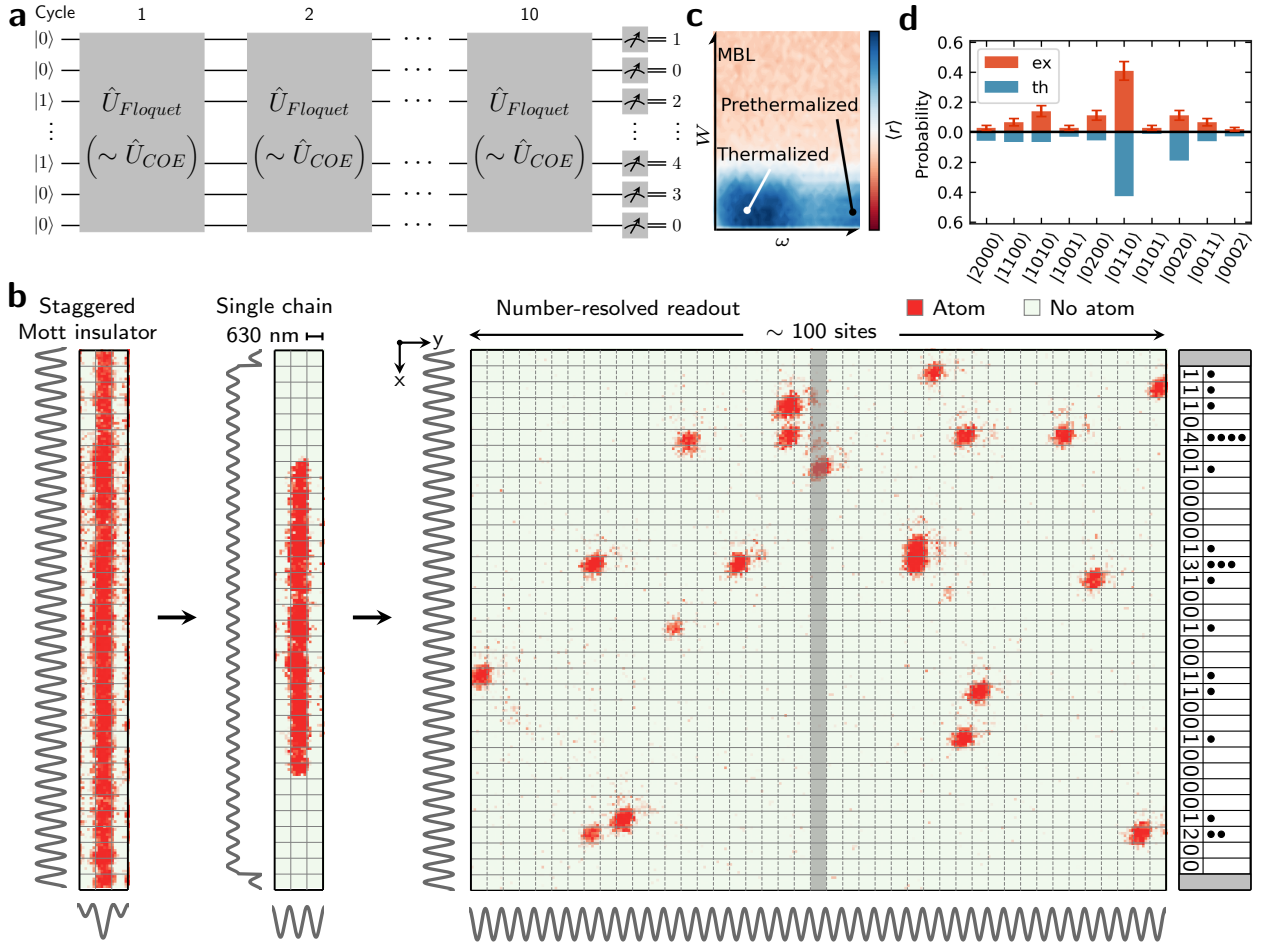


FIG. 1. **Sampling on a Floquet many-body system.** **a**, Quantum circuit illustration of the experiment. After ten cycles of the Floquet unitary evolution, we sample the output of the final states on the Fock basis. **b**, We implement the protocol in our analogue quantum simulator based on the quantum gas microscope set-up. First, a defect-free Mott insulator is prepared via staggered cooling. Utilizing the site-resolved addressing, we cut a single chain with N_b particles in the centre. Then the system evolves under a driven Bose-Hubbard model to the final states. The edges of the system are fixed by a box trap imposed by a DMD, forming a one-dimensional chain with L sites in the x direction. Before detection, we expand the atoms in the y direction over 100 sites, which circumvents the pair-wise loss of multiple atoms trapped in a single site during fluorescence imaging. **c**, The phase diagram of a driven Bose-Hubbard chain. For low driving frequency and weak disorders, the system will thermalize after several cycles of driving. If the intensity of the disorder increases, the thermalization breaks down and the system arrives at a MBL phase. **d**, The probability distribution estimated from the collected samples of the $L = 4$, $N_b = 2$ system. The error bars come from the Poisson statistics.

the small system's size up to 20 sites which can still be classically simulated and verifiable, we validate the samples via classical fidelity [25–30] or Bayesian hypothesis tests [23, 24]. These results from the Bayesian hypothesis tests can also be extrapolated to ensure that the system operates in the driven thermalized phase in the classically intractable regime. In the system of 32 sites with 20 atoms, the time cost is estimated to be at least 2,500 seconds to generate a single sample for the *Frontier* supercomputer (8,730,112 cores, 9.2 petabytes), the currently most powerful supercomputer worldwide, with the currently known best algorithms and supposing its random access memory (RAM) is sufficient (the

required RAM is much larger than that in the *Frontier*. See Supplementary Information). For comparison, it takes only 500 seconds to perform the same task in our quantum machine. The bichromatic superlattices allow us to measure the second-order Rényi entropy and monitor its real-time dynamics during the driving, which unveils a volume law of the entanglement in the driven thermalized phase. The multi-point correlation functions are extracted microscopically and enhanced high-order correlations are observed in the thermalized phase. These observations provide distinctions between the thermalized phase versus the MBL phase.

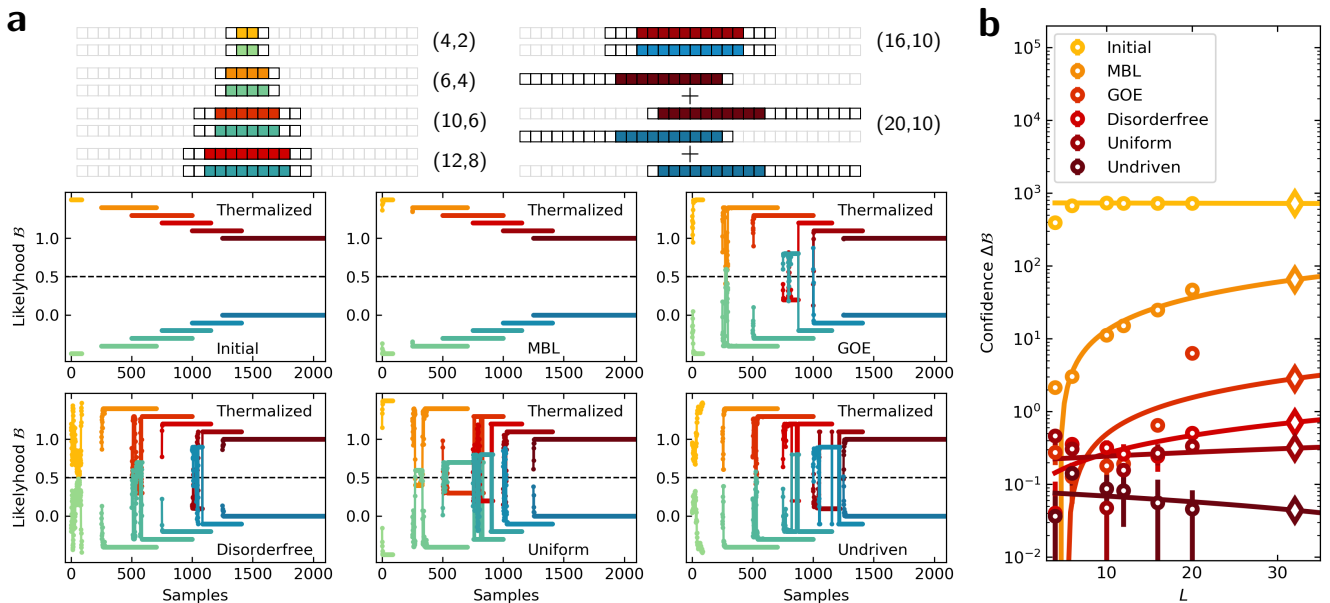


FIG. 2. **Bayesian tests.** **a**, Bayesian tests against 6 mock-ups, including initial, MBL, Gaussian orthogonal ensemble (GOE), Disorder-free, Uniform, and Undriven (middle and bottom panels, left to right). In each panel, we plot two curves of $\mathcal{B}(\text{ideal}, \text{mk})$ (hot color series) and $\mathcal{B}(\text{mk}, \text{ideal})$ (cold color series). For all the sampling sets, $\mathcal{B}(\text{ideal}, \text{mk}) > 0.5$ and approaches unity ($\mathcal{B}(\text{mk}, \text{ideal}) < 0.5$ and approaches zero) so the experimental samples passed all the tests, indicating that the samples are more likely generated by the target thermalized phase. To clearly show the curves, we displace them in both axes. **b**, The confidences of the Bayesian tests. All the confidences are positive (open circles) in the verifiable regime below 20 sites. Error bars are the standard error of the mean (SEM) and are smaller than the circles if being hidden. We linearly extrapolate the confidence (solid lines) to the largest size of $L = 32$, $N_b = 20$ (open diamonds).

Experimental set-up. Our experiment starts with a two-dimensional Bose–Einstein condensate of ^{87}Rb atoms polarized in state $|F = 1, m_F = -1\rangle$, which resides in a single anti-node of the vertical lattice (z lattice). Before ramping up the horizontal short lattices, we superimpose a staggered potential in the y direction by introducing a long lattice, whose wavelength is double that of the short lattice [31]. Then, we ramp up the xy short lattices to drive the phase transition to the Mott insulator. During the ramping, the entropy redistribution induced by the staggered potential renders the Mott insulator nearly defect-free (Fig. 1(b)) [32]. A site-resolved addressing beam is projected to the atoms through the objective by a digital micromirror device (DMD). We select a single chain along the x direction with a definite atom number N_b , and the rest of the atoms are pushed out by a resonant laser pulse.

Then, we drop the x short lattice depth to $2.9E_{r,S}$ to initialise the dynamics, where $E_{r,S} = \hbar^2/(8ma_S^2)$ is the recoil energy of the short lattice, m is the atomic mass of ^{87}Rb and $a_S = 630$ nm denotes the lattice constant of the short lattice. The length of the chain L is defined by imposing a box trap in the x direction (Supplementary Materials).

To periodically drive the system, the depth of the y short lattice is modulated following a sinusoidal curve $V_y(t) = V_y(1 + V_s \sin 2\pi\omega t)$, where $V_y = 47E_{r,S}$ is the

depth of the y short lattice and $V_s = 0.2$ is the amplitude of the modulation. At such a low depth of the x short lattice, the system can be described by the non-standard Bose-Hubbard model (NSBHM) [33]:

$$\begin{aligned} \hat{\mathcal{H}}_{NS} = & \hat{\mathcal{H}}_{BH} - T(t) \sum_i \left[\hat{b}_i^\dagger (\hat{n}_i + \hat{n}_{i+1}) \hat{b}_{i+1} + H.c. \right] \\ & + \frac{P(t)}{2} \sum_i \left(\hat{b}_i^{\dagger 2} \hat{b}_{i+1}^2 + H.c. \right) + U_2(t) \sum_i \hat{n}_i \hat{n}_{i+1} \\ & - J_2 \sum_i \left(\hat{b}_i^\dagger \hat{b}_{i+2} + H.c. \right), \end{aligned} \quad (1)$$

where $\hat{\mathcal{H}}_{BH} = -J \sum_i (\hat{b}_i^\dagger \hat{b}_{i+1} + H.c.) + U(t)/2 \sum_i \hat{n}_i (\hat{n}_i - 1) + W \sum_i h_i \hat{n}_i$ is the standard Bose-Hubbard model. W is the amplitude of the disorder potential and the random value h_i of the i -th site is obtained from the quasi-periodic lattice (Supplementary Materials). In the non-standard Bose-Hubbard model, T is the density-induced tunnelling, P is the pair tunnelling, U_2 is the nearest-neighbour interaction, and J_2 denotes the next-nearest-neighbour tunnelling. The modulation of the y lattice induces driving terms to those interaction-relevant terms, including U , T , P and U_2 .

Depending on the driving frequency and disorder, there exist three phases: driven thermalized, MBL

and prethermalized phases (Fig. 1(c)). What we are interested in is the thermalized phase, which supports the demonstration of quantum advantage. The chosen parameters are $J/h = 166(1)$ Hz, $U/h = 422(1)$ Hz, $\omega = 200$ Hz, and $W/h = 200$ Hz, where h is Planck's constant, lying in the driven thermalized phase. To eliminate the pairwise loss due to photo-association in fluorescence imaging, we expand the atoms in the y direction before imaging [34].

Classical fidelity. We measure the classical fidelity of the output probability distribution of the quantum machine. Classical fidelity is widely used in boson sampling experiments [25–30], which characterizes the overlap between the probability distribution of the experimental samples and the ideal probability distribution. It is defined as $F_c = \sum_i \sqrt{p_i q_i}$, where p_i is the ideal probability distribution and q_i the one inferred from the statistics of the samples obtained in experiments. In addition, the associated total variance distance between the probability distributions is defined as $d = 1/2 \sum_i |p_i - q_i|$. For $L = 4$ and $N_b = 2$, the dimension of the Hilbert space is 10, which allows efficient reconstruction of the probability distribution in experiments. The extracted values are $F_c = 0.981 \pm 0.053$ and $d = 0.153 \pm 0.053$ (Fig. 1(d)), indicating that the preparation and evolution in the experiments are well captured by the model Eq. 1. These values are comparable with those in boson sampling experiments [25–29]. Please note that the finite sampling effect reduces F_c even for samples generated from the ideal probability distribution [25]. Thus, the fidelity reported here is underestimated.

Bayesian test. Next, we explore the larger systems. In these cases, the samples are sparse compared to the dimension of the Hilbert space. To validate the quantum machine, we perform Bayesian hypothesis tests against a series of mock-ups. This Bayesian method has been used to validate the performance of large-scale boson sampling experiments [23, 24]. For an ideal probability distribution P_{ideal} and a mock-up one P_{mk} , we test the likelihood of the samples from the two probability distributions. Specifically, we define a ratio of the Bayesian likelihood $\mathcal{B}(\text{ideal}, \text{mk})$ as:

$$\mathcal{B}(\text{ideal}, \text{mk})_n = \frac{\prod_i^n P_{\text{ideal}}(S_i)}{\prod_i^n P_{\text{ideal}}(S_i) + \prod_i^n P_{\text{mk}}(S_i)}, \quad (2)$$

where n is the number of the samples and S_i is an instance of the samples. A likelihood ratio $\mathcal{B}(\text{ideal}, \text{mk}) > 0.5$ means that the samples are more likely generated from the ideal sampler rather than the mock-up sampler.

We present six relevant mock-ups and find that the experimental samples are more likely from the driven thermalized sampler (ideal sampler) rather than all these mock-up samplers for varied sizes of the system (see Fig. 2(a)). After dozens of samples, the likelihoods converge to unity, ruling out the mock-ups. To gain further information about the

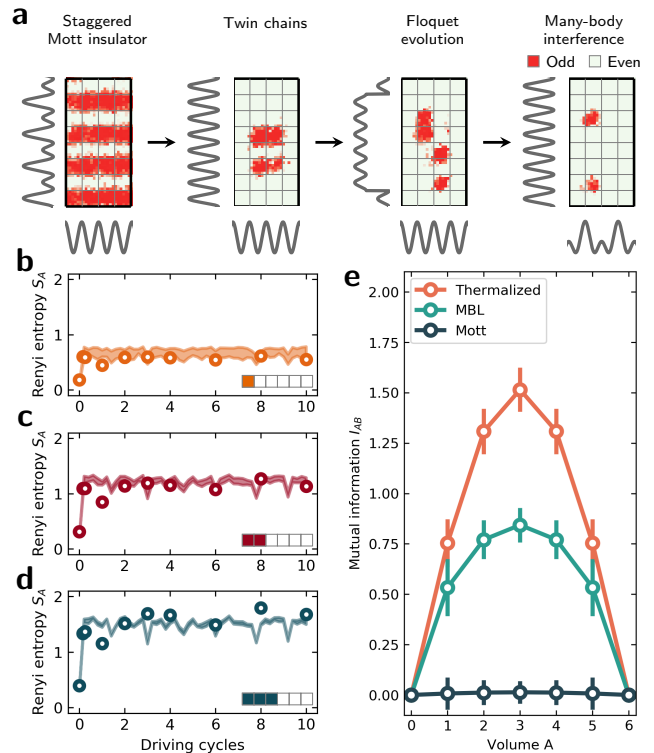


FIG. 3. Entanglement entropy. **a**, Schematics of the many-body interferometer. To perform beam-split operations, we prepare two neighbouring copies of chains, each with 2 atoms in 6 sites. After independent evolution, we freeze the dynamics and then apply a double well potential by the y superlattice to perform many-body interference. Finally, the parity is read out to extract the second-order Rényi entropy. **b-d**, Dynamics of the entanglement entropy. The volume of the subsystem is one (b), two (c), and three (d) sites, respectively. The experimental data (open circles) agree with the simulation (shaded area). The entanglement data are averaged over all possible combinations of the subsystems. Error bars denote the SEM and are smaller than the circles if being hidden. The width of the shaded area corresponds to the SEM of the simulation. **e**, The entropy of the thermalized phase versus the volume of the subsystem obeys a volume law, whereas it is the area law for the MBL phase. For the simulation, we use the Hubbard parameters calibrated from experiments without any free parameters.

likelihood, we introduce the confidence of the Bayesian test $\Delta\mathcal{B}(\text{ideal}, \text{mk})_n = \log [\prod_i^n P_{\text{ideal}}(S_i) / \prod_i^n P_{\text{mk}}(S_i)]$, which is positive if the samples are more likely generated from the ideal sampler. For all the mock-ups, the confidences are positive in the classical verifiable regime of up to $L = 20$, $N_b = 10$. We extrapolate the confidences to the advantage regime of 32 sites (Fig. 2(b)) and find that the confidences are positive, inferring that the samples are more likely from the driven thermalized phase. Using Schrödinger evolution (SE) algorithm, it would take 2 months to obtain the confidence of the samples in the $L = 32$, $N_b = 20$ system

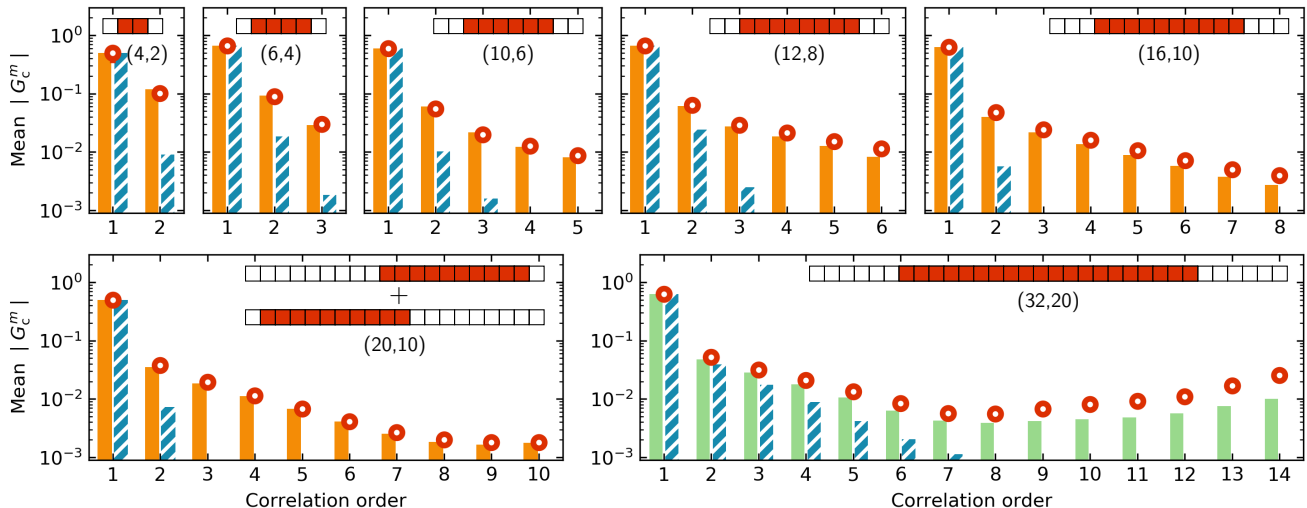


FIG. 4. **Multi-point correlation functions.** We extract multi-point density correlation functions from the experimental samples (open circles) for various sizes of the system. Correlations of up to 14th-order are shown. Error bars are the SEM and are hidden if smaller than the circles. Bars (slashed bars) denote the predicted value of the thermalized phase (MBL phase) from the SE simulations without any free parameters. The average value of $|G_c^m|$ takes over all the possible combinations of the subsystems. For the largest system of $L = 32$, $N_b = 20$, the predicted values are from a TDVP simulation with a bond dimension of 200. Since the combinatorial numbers and Bell numbers in this system are too large, we randomly select 100 subsystems with 14 sites to evaluate the mean value of the correlations. The smaller correlations of higher orders of thermalized phase predicted by the TDVP numerics in system (32,20) are attributed to the cut-off of the bond dimension, which includes less entanglement.

on *Hanhai20* clusters (28,800 cores, 138 terabytes) at USTC if the memory resources are sufficient. Even in the currently available fastest supercomputer, *Frontier*, the task of obtaining a sample would take 2,500 seconds. The quantum speedup on the sampling task is 5-fold compared to the *Frontier* supercomputer. Although the quantum advantage demonstrated here is moderate and there are possible improvements of classical algorithms to reduce the cost in the future, we still expect that the quantum-classical gap will be enlarged consistently by upgrades of larger quantum processors.

Entanglement entropy. A key feature of chaotic dynamics is the fast scrambling of entanglement. We perform many-body interference [34, 35] to measure the second-order Rényi entanglement entropy $S_2^A = -\ln \text{Tr}(\rho_A^2)$, where ρ_A is the reduced density matrix of subsystem A . Two copies of the chain are selected by the addressing beam. After driving for a varied number of cycles, we freeze the dynamics by ramping up the x short lattice to $51E_{r,s}$. Then the y long lattice is ramped up, implementing a balanced double well together with the lowered y short lattice for the many-body interference (Fig. 3(a)). After finishing the beam splitter operation, we freeze the dynamics in the y direction and image the atoms without expanding. The parity of the output in two ports could be obtained microscopically, from which we extract the purity and entanglement entropy on various sizes of the subsystems.

Fig. 3 shows the entanglement dynamics during driving. The entanglement increases and saturates quickly within a single driving cycle, which is expected by the eigenstate thermalization hypothesis (ETH) [34]. We further study the size dependence of the entanglement entropy. The mutual information defined as $I_{AB} = S_2^A + S_2^B - S_2^{AB}$ is used widely in condensed matter physics and quantum information science. In the thermalized phase, we observe a volume law of the mutual information (Fig. 3(e)), suggesting that there is no efficient matrix product state (MPS) representation for highly entangled states as the size of the system grows [9]. In contrast, it obeys an area law in the MBL phase, which is tractable with MPS for larger system sizes on classical computers.

Multi-point density correlation functions. Based on the sampling results, we further analyse the multi-point correlation functions [11, 23, 36–39] of the many-body system. In a Floquet system, multi-particle interactions emerge, which marks the breakdown of the Magnus expansion [7, 8, 40] and leads to enhanced high-order correlations. We exploit the multi-point density correlations to probe the many-body nature of the system. For the two-point case, $G_c^2(x_1, x_2) = G_{\text{tot}}^2(x_1, x_2) - G_{\text{dis}}^2(x_1, x_2) = \langle \hat{n}_1 \hat{n}_2 \rangle - \langle \hat{n}_1 \rangle \langle \hat{n}_2 \rangle$. Higher-order m -point multi-correlation functions of density are defined recur-

sively as:

$$G_c^m(\mathbf{x}) = G_{\text{tot}}^m(\mathbf{x}) - G_{\text{dis}}^m(\mathbf{x}), \quad (3)$$

where $G_c^m(\mathbf{x})$ is the connected correlation function applying to sites \mathbf{x} , and $G_{\text{dis}}^m(\mathbf{x})$ denotes the contributions of all the lower-order correlations (Supplementary Materials).

From the atom-number-resolved readout, we extract multi-point correlations up to 14th-order in the largest size of $L = 32$. The connected correlations are genuine many-body correlations, signalling the multipartite entanglement [38]. As shown in Fig. 4, the enhanced higher-order correlations in the thermalized phase contrasts with those in the MBL phase. The experimental data are consistent with predictions from simulations of the SE in systems below 20 sites. Above that, it is infeasible for the SE algorithm. Therefore, we employ the time-dependent variational principle (TDVP) algorithm for the classical simulation in the 32-site system. We find that the predicted values from the TDVP simulations are smaller than the experimental data. This deviation is attributed to the cut-off of the bond dimension in the TDVP simulation which involves less entanglement and cannot capture the higher-order correlations (Supplementary Materials). Moreover, higher-order correlations are impossibly accessed by samples generated by mock-up samplers merely containing lower-order correlations

[23]. This evidence further verifies the hardness for classically simulating this many-body system.

Conclusion and outlook. In summary, we experimentally characterized the thermalized phase of a driven many-body system via entanglement entropy and high-order correlations. This work establishes the utility of optical lattice quantum simulators for quantitative investigations on many-body dynamics beyond the capability of classical computation, opening the door for practical quantum advantage with noisy intermediate-scale quantum devices [10]. For future experiments, one can scale up the size of the problem straightforwardly by generalising to a two-dimensional system or introducing two types of bosons with different internal states. The optimal experimental parameters could be found via Hamiltonian learning [41–43] in a much larger dimension of the Hilbert space. Based on the programmabilities of the disorder and driving, we could explore the emergent geometries of the system [44] from the multi-point correlations in the quantum machine. In addition, the celebrated level statistics of the MBL and thermalized phases could also be probed via many-body spectroscopy [45].

-
- [1] Zhang, J. *et al.* Observation of a discrete time crystal. *Nature* **543**, 217–220 (2017).
- [2] Choi, S. *et al.* Observation of discrete time-crystalline order in a disordered dipolar many-body system. *Nature* **543**, 221–225 (2017).
- [3] Bluvstein, D. *et al.* Controlling quantum many-body dynamics in driven Rydberg atom arrays. *Science* **371**, 1355–1359 (2021).
- [4] Su, G.-X. *et al.* Observation of unconventional many-body scarring in a quantum simulator. arXiv:2201.00821.
- [5] D’Alessio, L. & Rigol, M. Long-time behavior of isolated periodically driven interacting lattice systems. *Phys. Rev. X* **4**, 041048 (2014).
- [6] Lazarides, A., Das, A. & Moessner, R. Equilibrium states of generic quantum systems subject to periodic driving. *Phys. Rev. E* **90**, 012110 (2014).
- [7] Ponte, P., Chandran, A., Papić, Z. & Abanin, D. A. Periodically driven ergodic and many-body localized quantum systems. *Ann. Phys.* **353**, 196–204 (2015).
- [8] Thanasilp, S., Tangpanitanon, J., Lemonde, M.-A., Dagniam, N. & Angelakis, D. G. Quantum supremacy and quantum phase transitions. *Phys. Rev. B* **103**, 165132 (2021).
- [9] Schuch, N., Wolf, M. M., Verstraete, F. & Cirac, J. I. Entropy scaling and simulability by matrix product states. *Phys. Rev. Lett.* **100**, 070502 (2008).
- [10] Daley, A. J. *et al.* Practical quantum advantage in quantum simulation. *Nature* **607**, 667–676 (2022).
- [11] Schweigler, T. *et al.* Experimental characterization of a quantum many-body system via higher-order correlations. *Nature* **545**, 323–326 (2017).
- [12] Feynman, R. P. Simulating physics with computers. *Int. J. Theor. Phys.* **21**, 467–488 (1982).
- [13] Preskill, J. Quantum computing and the entanglement frontier. *Rapporteur Talk at the 25th Solvay Conference on Physics, Brussels* (2012).
- [14] Flannigan, S. *et al.* Propagation of errors and quantitative quantum simulation with quantum advantage. arXiv:2204.13644.
- [15] Terhal, B. M. Quantum error correction for quantum memories. *Rev. Mod. Phys.* **87**, 307–346 (2015).
- [16] Georgescu, I. M., Ashhab, S. & Nori, F. Quantum simulation. *Rev. Mod. Phys.* **86**, 153–185 (2014).
- [17] Altman, E. *et al.* Quantum simulators: Architectures and opportunities. *PRX Quantum* **2**, 017003 (2021).
- [18] Tangpanitanon, J., Thanasilp, S., Lemonde, M.-A., Dagniam, N. & Angelakis, D. G. Quantum supremacy in driven quantum many-body systems. arXiv:2002.11946.
- [19] Arute, F. *et al.* Quantum supremacy using a programmable superconducting processor. *Nature* **574**, 505–510 (2019).
- [20] Wu, Y. *et al.* Strong quantum computational advantage using a superconducting quantum processor. *Phys. Rev. Lett.* **127**, 180501 (2021).
- [21] Zhu, Q. *et al.* Quantum computational advantage via 60-qubit 24-cycle random circuit sampling. *Sci. Bull.* **67**, 240–245 (2022).
- [22] Zhong, H.-S. *et al.* Quantum computational advantage using photons. *Science* **370**, 1460–1463 (2020).
- [23] Zhong, H.-S. *et al.* Phase-programmable gaussian bo-

- son sampling using stimulated squeezed light. *Phys. Rev. Lett.* **127**, 180502 (2021).
- [24] Madsen, L. S. *et al.* Quantum computational advantage with a programmable photonic processor. *Nature* **606**, 75–81 (2022).
- [25] Spring, J. B. *et al.* Boson sampling on a photonic chip. *Science* **339**, 798–801 (2013).
- [26] Tillmann, M. *et al.* Experimental boson sampling. *Nat. Photon.* **7**, 540–544 (2013).
- [27] Crespi, A. *et al.* Integrated multimode interferometers with arbitrary designs for photonic boson sampling. *Nat. Photon.* **7**, 545–549 (2013).
- [28] Carolan, J. *et al.* On the experimental verification of quantum complexity in linear optics. *Nat. Photon.* **8**, 621–626 (2014).
- [29] Wang, H. *et al.* High-efficiency multiphoton boson sampling. *Nat. Photon.* **11**, 361–365 (2017).
- [30] Zhong, H.-S. *et al.* 12-Photon entanglement and scalable scattershot boson sampling with optimal entangled-photon pairs from parametric down-conversion. *Phys. Rev. Lett.* **121**, 250505 (2018).
- [31] Li, M.-D. *et al.* High-powered optical superlattice with robust phase stability for quantum gas microscopy. *Opt. Express* **29**, 13876 (2021).
- [32] Yang, B. *et al.* Cooling and entangling ultracold atoms in optical lattices. *Science* **369**, 550–553 (2020).
- [33] Dutta, O. *et al.* Non-standard Hubbard models in optical lattices: a review. *Reports Prog. Phys.* **78**, 066001 (2015).
- [34] Kaufman, A. M. *et al.* Quantum thermalization through entanglement in an isolated many-body system. *Science* **353**, 794–800 (2016).
- [35] Islam, R. *et al.* Measuring entanglement entropy in a quantum many-body system. *Nature* **528**, 77–83 (2015).
- [36] Hodgman, S. S., Dall, R. G., Manning, A. G., Baldwin, K. G. H. & Truscott, A. G. Direct measurement of long-range third-order coherence in Bose-Einstein condensates. *Science* **331**, 1046–1049 (2011).
- [37] Dall, R. G. *et al.* Ideal n-body correlations with massive particles. *Nat. Phys.* **9**, 341–344 (2013).
- [38] Rispoli, M. *et al.* Quantum critical behaviour at the many-body localization transition. *Nature* **573**, 385–389 (2019).
- [39] Koepsell, J. *et al.* Microscopic evolution of doped Mott insulators from polaronic metal to Fermi liquid. *Science* **374**, 82–86 (2021).
- [40] Magnus, M. On the exponential solution of differential equations for a linear operator. *Commun. Pure Appl. Math.* **7**, 649 (1954).
- [41] Wang, J. *et al.* Experimental quantum Hamiltonian learning. *Nat. Phys.* **13**, 551–555 (2017).
- [42] Bairey, E., Arad, I. & Lindner, N. H. Learning a local Hamiltonian from local measurements. *Phys. Rev. Lett.* **122**, 20504 (2019).
- [43] Li, Z., Zou, L. & Hsieh, T. H. Hamiltonian tomography via quantum quench. *Phys. Rev. Lett.* **124**, 160502 (2020).
- [44] Periwal, A. *et al.* Programmable interactions and emergent geometry in an array of atom clouds. *Nature* **600**, 630–635 (2021).
- [45] Roushan, P. *et al.* Spectroscopic signatures of localization with interacting photons in superconducting qubits. *Science* **358**, 1175–1179 (2017).

Acknowledgements We thank Pan Zhang for help-

ful discussions. This work was supported by the National Natural Science Foundation of China (Grant No. 12125409), the Innovation Program for Quantum Science and Technology (2021ZD0302000), and the Anhui Initiative in Quantum Information Technologies. We thank the USTC supercomputing center for providing computational resources for this project.

SUPPLEMENTARY MATERIALS

CONTENTS

1. Experimental sequences and techniques	9
1.1. Sequence for sampling experiments	9
1.2. Sequence for entanglement entropy experiments	9
1.3. Measurement of entanglement entropy via many-body interference	9
2. Calibrations of Hubbard parameters	10
2.1. Tunnelling and on-site interaction	10
2.2. Dipole potentials imposed by DMDs	11
2.3. Local energy offset	11
3. Non-standard Bose-Hubbard model	12
3.1. Non-standard terms	12
3.2. Comparison with BHM	13
3.3. Finite-sampling effect	13
4. Theoretical evidence of quantum advantage signatures in sampling from the driven thermalized quantum systems	13
4.1. Computational complexity of sampling from COE dynamics	14
4.2. Implication to the driven thermalized systems	14
5. Classical Algorithms	15
5.1. Schrödinger evolution	15
5.2. Time-dependent variational principle	16
5.3. Comparison of the numerics	16
6. Data analysis	16
6.1. Sample collection	16
6.2. Mock-up distributions	16
6.3. Multi-point correlation functions	17

1. EXPERIMENTAL SEQUENCES AND TECHNIQUES

1.1. Sequence for sampling experiments

Our experiments begin with a two-dimensional Bose-Einstein condensate of ^{87}Rb atoms in the $5S_{1/2}$ [$F = 1, m_F = -1$] state, which is trapped in a single antinode of the z lattice [46]. The sequence used to draw samples from the thermalized phase is illustrated in Fig. S1(a).

Initial state preparation. During the transition from superfluid to Mott insulator, we perform staggered cooling to obtain a Mott insulator with nearly unity filling [32]. The staggered potential is applied by the y long lattice, whose trap minima overlap with the minima of the y short lattice. To compensate for the overall envelope induced by red-detuned lattices, we project a blue-detuned anti-trapping potential with DMD1. The average filling is approximately 0.75 so that the filling is unity in the Mott chains and 0.5 in the reservoir chains, respectively. After the phase transition, we further ramp up the xy short lattices and the z lattice to above $90E_{rS}$. Then we shift the minima of the y long lattice to overlap with the maxima of the y short lattice and turn on the spin-dependent effect by rotating the polarizations of the lattice beams to introduce a differential light shift between $|F = 1, m_F = -1\rangle$ and $|F = 2, m_F = -2\rangle$ [47]. The splitting of the resonant frequency between the Mott chains and reservoir chains is 12 kHz. After selectively flipping the atoms in the reservoir chains, we push out the atoms with a resonant laser of the cycling transition and only the atoms in the Mott chains are retained. After that, we impose an addressing beam with a magical wavelength ($\lambda = 787.55$ nm) projected by DMD2 to shift the resonant frequency by 12 kHz between the $|F = 1, m_F = -1\rangle$ and $|F = 2, m_F = -2\rangle$ states of the addressed atoms [48, 49]. We flip the bare atoms to $|F = 2, m_F = -2\rangle$ and push out them, akin to cleaning atoms in the reservoir chains. As a result, we deterministically prepare the initial $1 \times N_b$ state in a single chain. Then the retained atoms are flipped to the $|F = 2, m_F = -2\rangle$ state for the following experiments.

Driven dynamics evolution. We then initialise the driving process by suddenly quenching the x lattice to $2.9E_{rS}$ and modulating the y lattice at the same time. The amplitude of the modulation is $9.4E_{rS}$. The depth of the y lattice is $47E_{rS}$, so tunnelling in this direction is suppressed. A box trap along the x direction projected by DMD3 confines the atoms in L sites during the evolution. In addition, we also remove the inhomogeneities of the chemical potential induced by red-detuned lasers as we did in the superfluid-Mott insulator transition. The disorder potential is applied before the evolution. After ten cycles of driving, we freeze the dynamics by ramping up the x lattice to $51E_{rS}$.

Full-count detection. Due to the light-assisted collisions [50], we could only detect the parity of the atomic

occupation in fluorescence imaging. To obtain the full count of the final state, we expand the atoms in the y direction by dropping down the y lattice to $0.1E_{rS}$ [34]. After a time of 2 ms of free tunnelling in the y direction, we pin the atoms to perform fluorescence imaging. Finally, we obtain the samples of the state in an atom-number-resolved way.

1.2. Sequence for entanglement entropy experiments

To measure the second-order Rényi entropy, we need to perform many-body interference on two copies. The twins should be prepared in adjacent chains, i.e., in a single double-well formed by the y superlattice. Therefore, we perform the staggered cooling in the x direction instead of the y direction which will result in an alternating structure of the atoms in the y direction.

The sequence to measure the entanglement entropy is illustrated in Fig. S1(b).

Initial state preparation. After staggered cooling and pushout of the reservoir chains, we impose an addressing beam to select a 2×6 plaquette region. As a result, we create two adjacent chains of state $|001010\rangle$ in the x direction.

Beam splitter operation and parity readout. After finishing the driving, we ramp up the x lattice to freeze the dynamics. Then the y long lattice is ramped up to $9.3E_{rS}$ and the y short lattice is ramped down to $19.8E_{rS}$, forming a balanced double well. To further reduce the on-site interaction, we lower the depths of the x short lattice and the z lattice to $26E_{rS}$ and $23E_{rS}$, respectively. The calculated tunnelling rate J_{BS}/h is 967 Hz, and the residue interaction U_{BS}/h is 402 Hz, yielding a contrast of 99% of the beam splitter operation. After performing a 50:50 beam splitter operation on the atoms [51], we freeze the atoms by ramping up the x short lattice. Finally, the atoms are pinned and imaged without expanding. The pair-wise loss during fluorescence imaging allows us to read out the parities of the sites.

1.3. Measurement of entanglement entropy via many-body interference

To calibrate the beam splitter operation, we monitor the tunnelling dynamics of the atom in the double well for both single-atom and two-atom cases. For single atom occupation, it oscillates between the wells with a frequency of $2J_{BS}/h$ as shown in Fig. S2(a). The measured tunnelling rate is $J_{BS}/h = 932(3)$ Hz, and the amplitude is 99(2)%. For the two-atom case, we extract the joint probability $P(1, 1)$ of finding two atoms in separate wells. The joint probability $P(1, 1)$ oscillates at a frequency of $\sqrt{64J_{BS}^2 + U_{BS}^2}/2h \approx 4J_{BS}/h$. As shown in Fig. S2(b), the oscillating frequency is 3704(1) Hz and the contrast is 96(3)%, which agrees with the prediction. At the minima

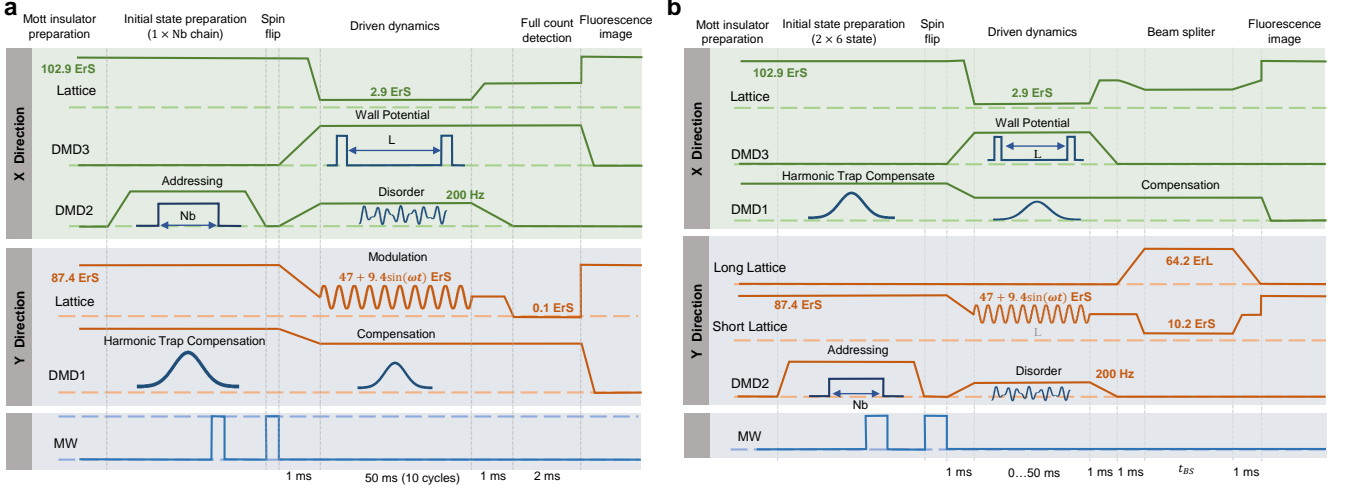


FIG. S1. **Experimental sequences.** **a**, Sequence for sampling in the driven thermalized phase of a Hubbard chain. **b**, Sequence for probing the entanglement entropy of the driven Hubbard chain.

of the oscillation, the two atoms are in a superposition of $|0, 2\rangle$ and $|2, 0\rangle$, corresponding to a 50 : 50 beam splitter operation. The first beam splitter time is used in the following experiments. At this time, the joint probability is $P(1, 1) = 0.04(2)$. The purity of the initial Fock state is estimated to be $\langle P_i \rangle = 1 - 2 \times P(1, 1) = 92(4)\%$, where i denotes the output ports, indicating a high fidelity of the beam splitter operation. The second-order Rényi entropy is directly related to the purity [51]

$$S_A^2 = -\ln \text{Tr}(\rho_A^2) = -\ln \langle P_i(A) \rangle, \quad (\text{S1})$$

where $\langle P_i(A) \rangle$ is the purity of subsystem A . These operations are not perfect and introduce extensively classical entropy to experimental data [34, 35, 52]. To compare with numerical simulations, we added an offset to the theoretical predictions in Fig. 3(c-d).

2. CALIBRATIONS OF HUBBARD PARAMETERS

2.1. Tunnelling and on-site interaction

We calibrate the tunnelling strength J and the on-site interaction strength U using methods similar to those described in Ref. [53]. The tunnelling J is measured at a depth of $2.9E_{rS}$, which is used in the experiments. For the measurement of interaction U , it is too shallow that atoms delocalize quickly even when applying a gradient of 30 G/cm in the x direction. Hence, the depth of the x short lattice is set to $10.4E_{rS}$ during the calibration of U . The modulation amplitude is $2.5E_{rS}$, and the duration of the modulation is 100 ms. The result is shown in Fig. S3(b). Two dips correspond to resonances at $\nu_1 = E_{\text{tilt}} + U$ and $\nu_2 = E_{\text{tilt}} - U$, where E_{tilt} is the tilt

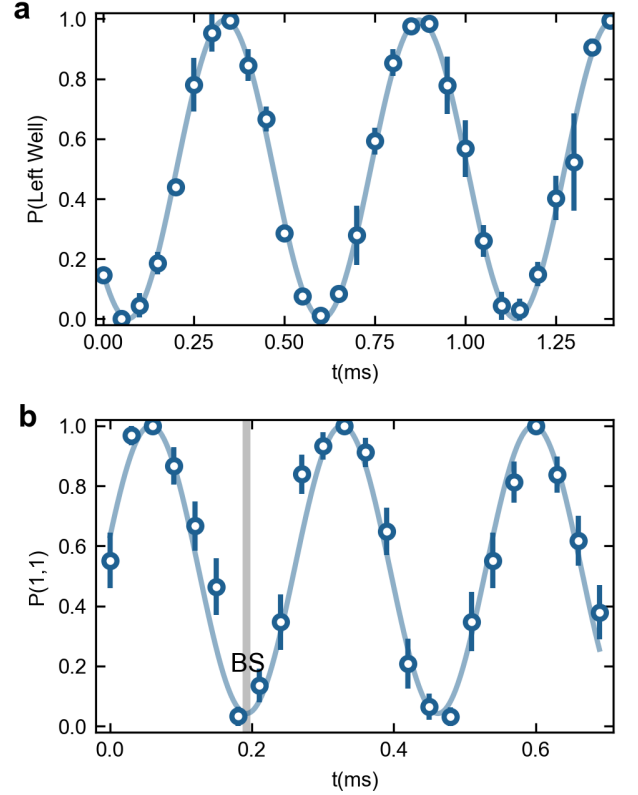


FIG. S2. **Dynamics of atoms in double well.** **a**, Single-atom tunnelling process. The atom is initially localized in the left well. **b**, Two-atom tunnelling process. The two atoms are initially localized in separate wells. The tunnelling processes start during ramping down of the y short lattice. Hence, the probability $P(\text{Left Well})$ and $P(1, 1)$ are not unity at $t = 0$.

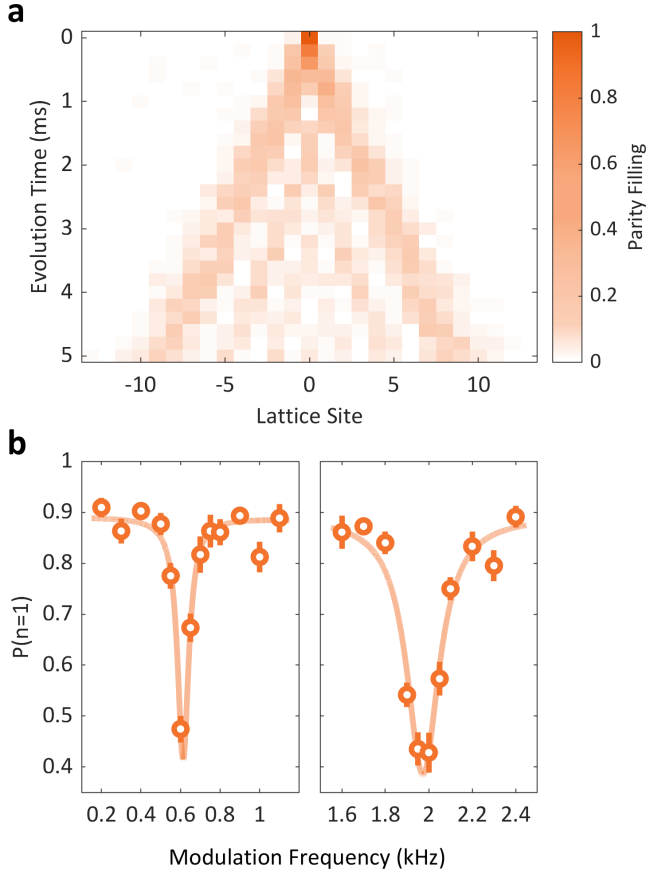


FIG. S3. **Calibrations of Hubbard parameters J and U .** **a**, Quantum walk of a single atom. The result shows $J/h = 166(1)$ Hz. **b**, Plot of the population fraction versus the modulation frequency. The result shows two expected dips at $E_{\text{tilt}} \pm U$ with $U/h = 680(4)$ Hz.

between two adjacent sites in the x direction induced by the magnetic gradient field. These results are consistent with the prediction from band calculations. Thus, the other terms included in the NSBHM are derived directly from the band calculations.

2.2. Dipole potentials imposed by DMDs

We use three DMDs in the experiments, which are labelled as DMD1, DMD2, and DMD3. DMD1 is used to compensate for the overall harmonic trapping potential induced by red-detuned lattices. DMD2 is used for addressing and imposing disorder potential. We utilise DMD3 to project a box trap for confining atoms during the driving dynamics.

DMD1. First, we measure the trapping frequency in the horizontal direction by observing the breathing mode oscillations of the atoms in 2D [55]. The frequency of the oscillation corresponds to twice the trapping frequency. Then, we project an anti-trapping pattern by DMD1 with a 750 nm laser to the atoms. The oscillation frequency

decreases as we increase the intensity of the laser (see Fig. S4(a,b)). We thus extrapolate the value of the intensity where the trapping frequency is zero, i.e., it is homogeneous in the horizontal direction.

DMD2. The wavelength of the addressing beam is 787.55 nm, and the polarization is circular, which constitutes one magical wavelength between the $D1$ and $D2$ transitions. There is no light shift to $|F = 1, m_F = -1\rangle$ yet a red shift to $|F = 2, m_F = -2\rangle$. The differential light shift between $|F = 1, m_F = -1\rangle$ and $|F = 2, m_F = -2\rangle$ could be obtained via microwave (MW) spectroscopy. We project a flattop pattern to the atoms and scan the MW frequency to flip the atoms to $|F = 1, m_F = -1\rangle$ before the pushout. The number of retained atoms maximises at the resonant frequency (see Fig. S4(c)).

The disorder potential is also imposed by the addressing beam with smaller intensity. The local energy offset is directly related to the extrapolated light shift since the atoms are in state $|F = 2, m_F = -2\rangle$. The disorder potential comes from a quasi-periodic lattice, which is given by

$$V_{\text{dis}}(x) = 2W \left\{ (2 - \beta) \cos^2 \left[\pi(\beta - 1) \frac{x}{a_S} + \phi \right] + (\beta - 1) \cos^2 \left[\pi(\beta - 2) \frac{x}{a_S} + \phi \right] \right\}, \quad (\text{S2})$$

where $\beta = (\sqrt{5} - 1)/2$ is the golden ratio. This type of disorder potential takes the advantage that it is flat in the lattice sites and is immune to the relative position drift between the DMD2 pattern and the lattice phase [53]. We choose three instances of disorder potentials with $\phi = 0.1\pi, 0.4\pi$ and 0.7π .

DMD3. DMD3 projects a box trap potential to confine the atoms during driving. The wavelength of the light is also 750 nm. The pattern of the wall is given by a flattop functions

$$I = \text{erf} \left(\frac{x - x_0 + \sigma_w}{\sigma_s} \right) + \text{erf} \left(-\frac{x - x_0 - \sigma_w}{\sigma_s} \right), \quad (\text{S3})$$

where $\text{erf}(\dots)$ is the Gaussian error function. The sharpness is determined by σ_s and $2\sigma_w$ is the width of the wall. To minimise the energy offset in the edge sites close to the wall, we optimise the wall by varying the sharpness. Fig. S4(f) shows the profile of the walls in the edge sites with different sharpness parameters. With the optimal value, the local energy offset in the edge sites is approximately 150 Hz while the height of the wall is $\sim 10E_{r,S}$. The width of the wall is 6 sites, suppressing atoms from tunnelling outside the walls.

2.3. Local energy offset

Even though the disorder potential could be monitored from the CMOS, the potential experienced by atoms is the combination of all the lattices and the projected

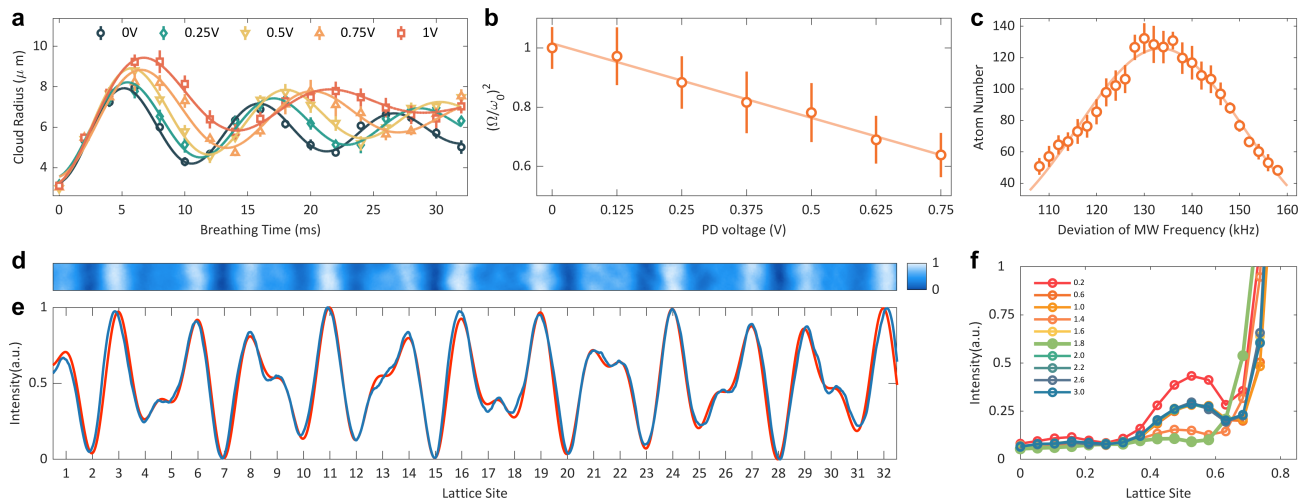


FIG. S4. **Calibration of potentials projected by DMDs.** **a**, Breathing-mode oscillations with different powers of the laser projected by DMD1. The solid curves are the fitting results from a damped sinusoidal function. **b**, The fitted breathing mode frequency ratios $(\Omega/\omega_0)^2$ and the DMD1 power have a linear relation, where ω_0 is the breathing mode frequency without the anti-trapping potential. **c**, Number of addressed atoms against the induced light shift. The solid curve is a Gaussian fitting, which yields the centre frequency at 125.8(3) kHz. **d**, Image of the disorder potential in 1×32 sites. **e**, Profile of the implemented disorder potential. The measured result (blue curve) is averaged over one site from the above image, which is overlapped with the target one (red curve). The slight deviation between two curves is attributed to the optical aberration and the finite size of the DMD pixels. **f**, Profile of the walls in one edge with different sharpness σ_s given by DMD3. The light green line with closed circles represents the optimal sharpness of $\sigma_s = 1.8$ pixels on the CMOS, which minimises the local energy offset to the edge sites.

lasers. Hence, we calibrate the potential in the atom plane via an *in situ* method. Thanks to the capability of the site- and number-resolved readout, we could extract the density profile of the chain, which depends on the chemical potential under local density approximation. The local energy shift at each site can be obtained from the self-consistent iterations until the error ϵ between the density profiles from the experiments and simulations is sufficiently small. We insert calibration shots during the collection of the samples. The calibration shots share the same parameters with the sampling experiments except without driving. For smaller sizes ($L \leq 16$), we exploit SE, and for $L \geq 20$, we use TDVP for the iteration, respectively. We have compared the density profiles given by SE and TDVP for smaller sizes and found that the deviations were negligible. In practice, we need dozens of iterations to converge at an error of $\epsilon < 0.02$ (see Fig. S5).

3. NON-STANDARD BOSE-HUBBARD MODEL

3.1. Non-standard terms

In our experiment, the lattice depth is as low as $2.9E_{rS}$ along the x direction. For such a shallow optical lattice, the Wannier functions are wider to cover neighbouring sites. The contributions of nearest-neighbour interactions and next-nearest-neighbour processes are not negligible. The NSBHM [33] includes these terms in addition

Term	Value (Hz)
nearest-neighbour tunnelling, J/h	166
on-site interaction, U/h	422
next-nearest-neighbour tunnelling, J_2/h	18
nearest-neighbour interaction, U_2/h	9
density-induced tunnelling, T/h	8
pair tunnelling, P/h	5

TABLE S1. **Parameters in the experiment.** These parameters are calculated for $V_x = 2.9E_{rS}$, $V_y = 47.0E_{rS}$ and $V_z = 45.4E_{rS}$

to J and U , as given in Eq. 1.

Fig. S6(a) illustrates all contributing processes in this model. Here, U_2 is the nearest-neighbour interaction, T is the density-induced tunnelling, P is the pair tunnelling, and J_2 denotes the next-nearest-neighbour tunnelling.

In Fig. S6(b), the amplitudes of these processes at different lattice depths along the x direction are shown. When $V_x = 2.9E_{rS}$, $V_y = 47.0E_{rS}$ and $V_z = 45.4E_{rS}$, the values of these processes are summarized in Table S1. We can find that at the experimental parameters, the additional terms are ~ 10 percent J . As the depth

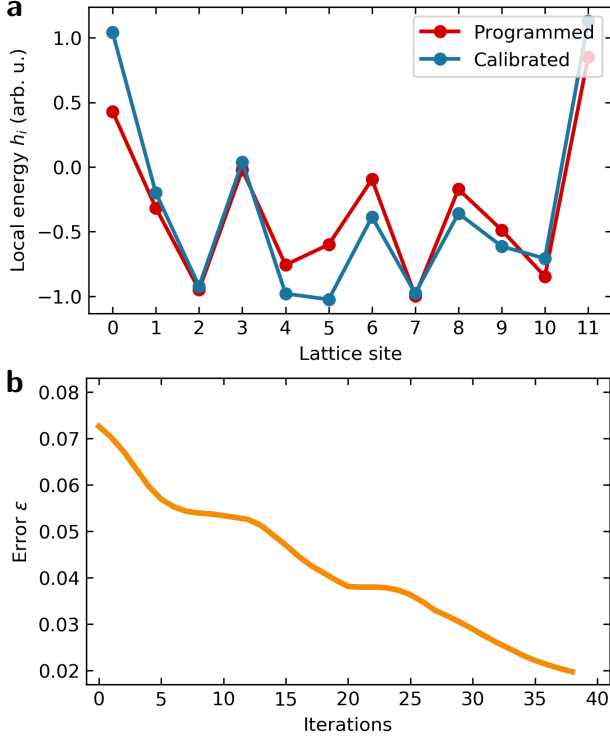


FIG. S5. **Calibration of chemical potential.** **a**, Red circles are programmed disorder potentials for a 12-site chain. Note that the boundary sites are lifted by the wall. Green circles are calibrated local potentials. The deviations between them are attributed to dipole potentials induced by other lasers. **b**, Error of density profile decreases versus iterations.

of the lattice increases, the non-standard processes are suppressed. When $V_x = 10E_{rS}$ or larger, the additional terms are two orders of magnitude smaller than J and U . Thus, for a deeper lattice, these terms could be dropped in the standard BHM.

3.2. Comparison with BHM

We compared the two models in the evaluations of the classical fidelity. First, we calibrate the chemical potential using the non-standard model and then calculate the ideal probability to evaluate the classical fidelity. The procedure is repeated with the standard Bose-Hubbard model. The chosen samples and experimental data for the chemical calibrations are identical, and J and U are the same in the non-standard BHM and the standard one. The former's fidelity is higher than the latter by ~ 2 percent, which indicates that the NSBHM capturing the additional processes is more suitable in the regime of experimental parameters.

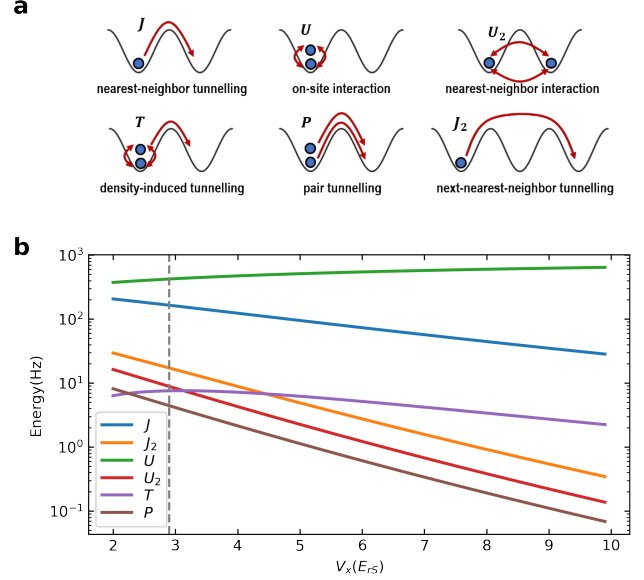


FIG. S6. **All processes in the non-standard Bose-Hubbard model.** **a**, J is the nearest-neighbour tunnelling, U is the on-site interaction, J_2 is the next-nearest-neighbour tunnelling, U_2 is the nearest-neighbour interaction, T is the density-induced tunnelling, and P is the pair tunnelling. **b**, The strengths of those processes in the NSBHM versus lattice depth. The additional processes are ~ 10 percent J at $V_x = 2.9E_{rS}$, while in deep lattices, they are two orders of magnitude smaller than J .

3.3. Finite-sampling effect

In the main text, we measure the classical fidelity F_c and the total variance distance d of the output probabilities for an $L = 4, N_b = 2$ system. The measurement results are $F_c = 0.981 \pm 0.053$ and $d = 0.153 \pm 0.053$, with 88 samples in total.

Fig. S7 reveals the finite-sampling effect on F_c and d [25]. We draw samples from the ideal probability distribution by a Monte-Carlo method without any noise. However, the classical fidelity is below 99% if the number of samples is less than 100. This means that the measured results in the main text are underestimated due to the finite-sampling effect.

4. THEORETICAL EVIDENCE OF QUANTUM ADVANTAGE SIGNATURES IN SAMPLING FROM THE DRIVEN THERMALIZED QUANTUM SYSTEMS

In this section, we provide a brief theoretical overview on signatures of a sampling quantum advantage in driven thermalized quantum many-body systems. For more details, we refer readers to Ref. [8].

We start by providing formal evidence that sampling output-strings from a periodic evolution of an unitary in-

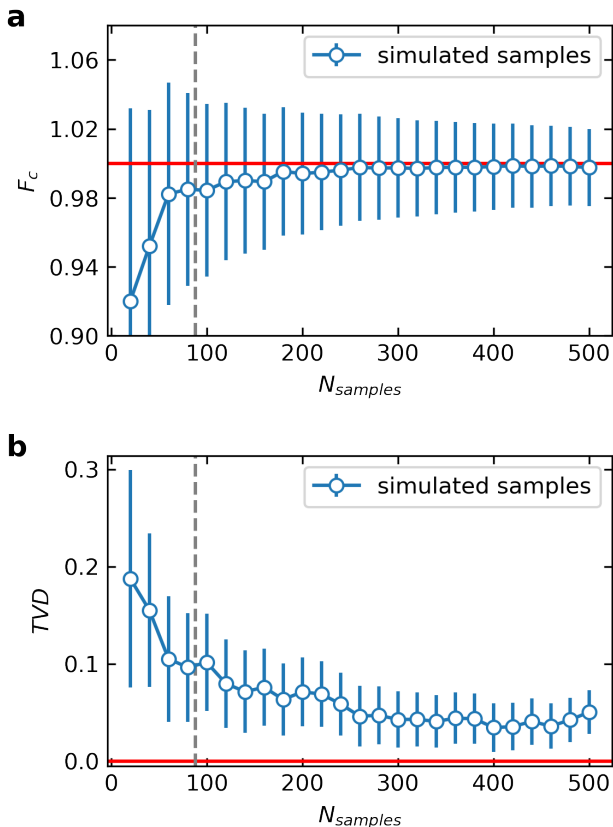


FIG. S7. F_c and d for simulated samples. **a**, F_c of different sample numbers. When there are 88 simulated samples, $F_c = 0.986 \pm 0.053$. **b**, Total variance distance (TVD) d of different sample numbers. When there are 88 simulated samples, $d = 0.094 \pm 0.053$. Error bars are the SEM. Red solid line is the upper limit (lower limit) for the fidelity (total variance distance).

stance drawn from COE cannot be achieved efficiently using classical computers unless polynomial hierarchy (PH) collapses. The PH non-collapse is a strongly-held conjecture in computer science community with the most famous example of $P \neq NP$. Then, we argue that, thanks to the intimate connection between COE and an ensemble of Floquet unitaries in the driven thermalized phase, this suggests the same sampling complexity could be expected in the driven thermalized quantum systems.

4.1. Computational complexity of sampling from COE dynamics

We first quickly introduce the standard procedure used to demonstrate a sampling quantum advantage in most proposals such as random quantum circuits [19]. Intuitively, all proposals of a sampling quantum advantage aim to generate quantum evolution that has a sufficient amount of randomness such that classical computers have no structure in the evolution to be exploited and are

required to simulate the entire Hilbert space, which is widely believed to be inefficient.

Given protocols to generate a random physical unitary \hat{U} , our first step is to assume that there exists a classical machine \mathcal{C} that can efficiently sample from the evolution generated by \hat{U} . If we are able to show that the unitaries constructed from the protocols satisfy the *anti-concentration* condition, the computational power of \mathcal{C} can be boosted using the Stock-Mayer theorem to *approximate* the output probability of the quantum evolution. Physically-speaking the anti-concentration implies that most of bit-strings have finite probabilities to be measured. Our upgraded classical machine now with the computational power to not only sample from the output distribution but also approximate the output distribution is said to reside in the third level of Polynomial Hierarchy. Our next step is to show that this task of approximating output distribution is $\#P$ -hard (preferably on average). Then, this would imply that our upgraded machine in the third level has an ability to efficiently solve a $\#P$ -hard task, leading to a collapse of Polynomial Hierarchy to the third level. Since it is strongly believed from the computational complexity perspective that the PH collapse cannot happen, the only way to rescue ourselves in this situation is to conclude that the classical machine \mathcal{C} does not exist in the first place.

As one can see, there are two key conditions to show before claiming a quantum advantage in sampling tasks. (i) multiplicative approximation of the output distribution is $\#P$ hard on average and (ii) anti-concentration of the output distribution. Ref [8] shows that indeed COE satisfies both conditions. The $\#P$ hardness is proven in the worst case scenario. Particularly, as IQP circuits are a part of COE family, this shows that there exists at least one instance in COE that is $\#P$ hard. The average case hardness is conjectured with some theoretical support by mapping from COE dynamics to complex Ising spin-chains. The anti-concentration is proven using the statistical properties of COE, showing the output distribution satisfies the Porter Thomas distribution.

4.2. Implication to the driven thermalized systems

Now, we discuss the consequences of our results obtained in the previous section for periodically driven quantum many-body systems in the thermalized phase. Particularly, COE and the ensemble of Floquet unitaries generated by the driven thermalized quantum systems are closely connected thanks to the external drive which increases the level of randomness in the physical systems. To understand how the external drive plays a role, we first consider the case of generic *undriven* thermalized systems. Here the quantum system thermalizes to finite temperature due to energy conservation. One can apply random matrix theory to accurately describe systems over narrow energy windows distant from the energy spectrum's boundaries. If the complete energy spec-

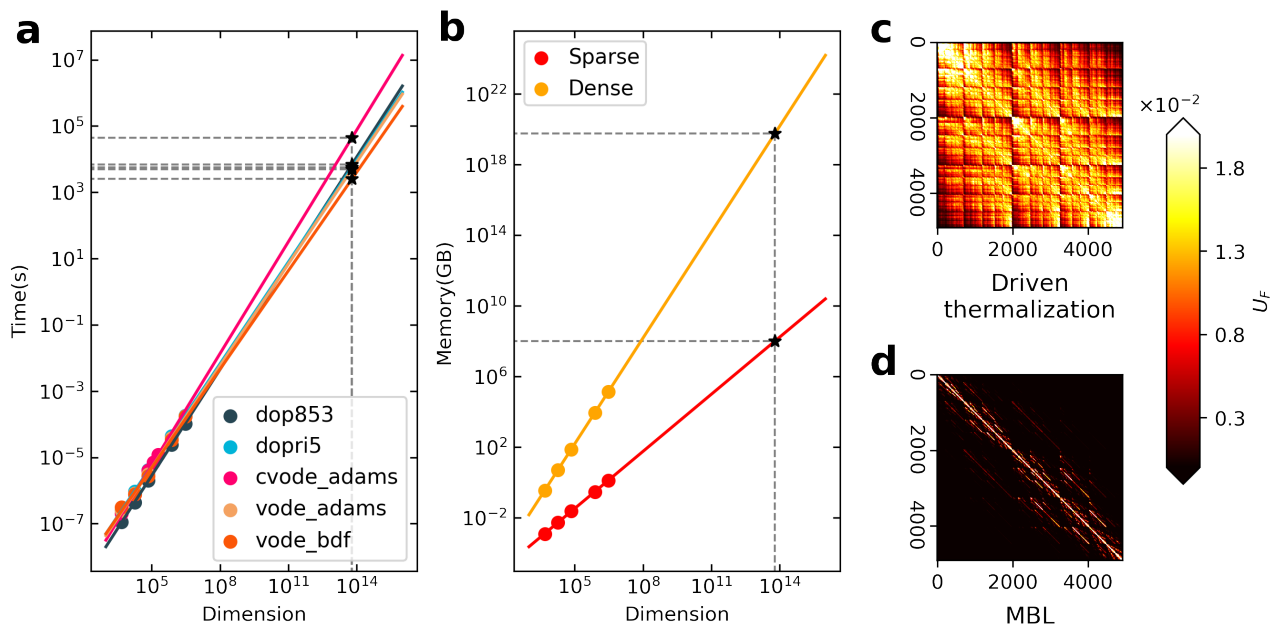


FIG. S8. **Cost of the classical algorithm.** **a**, The estimated time cost for the classical algorithms to solve the time-dependent Schrödinger equation on the *Frontier* supercomputer (blue dots). We compare several best-known ODE solvers. In larger system sizes, the *volve.bdf* method performs best in terms of time cost. The blue solid line is linear fitting for logarithms of dimension and time. **b**, The space complexity for varied system sizes. The orange and red dots denote the consumed storage memory required for sparse (non-zero elements) and dense (full elements) Hamiltonian matrices, respectively. The solid lines are linear fitting for logarithms of dimension and memory. **c** and **d** show the heat maps of a typical Floquet operator in terms of matrix element in the driven thermalized and MBL phases, respectively.

trum is analyzed, the local structure generally observed in static Hamiltonians emerges and random matrix theory is no longer valid. In addition, there are additional constraints due to local few-body interactions.

This is in contrast to the driven thermalized systems where random matrix theory can be accurately applied to the entire \hat{U}_F spectrum. Furthermore, under the condition that COE and the driven thermalized systems share the same statistical distributions as indicated by the Floquet ETH. Lastly, using Magnus expansion one can show that the Floquet Hamiltonian H_F has effective infinite-range multi-body interactions generated by the periodic drive. Consequently, the majority of restrictions from local interactions typically seen in physical systems are removed. Therefore, one can speculate the sampling complexity from the generic driven thermalized quantum systems to be the same as sampling from COE.

5. CLASSICAL ALGORITHMS

5.1. Schrödinger evolution

To solve the time-dependent Schrödinger equation, we adopt an open-source software package, *Quspin*, to compute the evolution of the driven system. Ref. [57] provides a detailed introduction to this package. The origi-

nal version of the package only involves the ordinary differential equation (ODE) solvers provided by *SciPy* [58]. We further added the *cvoke* solvers from the *Pyodesys* [59] to *Quspin*.

In Fig. S8(a), we plot the required time to solve the time-dependent Schrödinger equation for different system sizes. We first record the time spent on *Hanhai20* clusters (with Rpeak 2.38 PFlop/s) at USTC, then we estimate how long it will take on *Frontier* (with Rpeak 1,685.65 PFlop/s) by comparing floating-point computing power. The blue dots represent the time of systems within the computational capability of the *Hanhai20* clusters. We fit the curve and extrapolate it into the classically intractable regime to determine the required time of our largest system of $L = 32$, $N_b = 20$. When the dimension of the Hilbert space reaches $\sim 10^{14}$, the corresponding time to obtain one valid sample is $\sim 2,500$ s on *Frontier* employing the fastest solver of *volve.bdf*, while it takes only 500 s in our experiment.

Fig. S8(b) illustrates the allocated memory for storing the matrix elements of the sparse (red dots) and dense (orange dots) Hamiltonians. Here the sparse matrix denotes that the matrix contains only non-zero elements, while the dense matrix contains the full elements. For a system with approximately 10^{14} Hilbert space dimensions, storing the sparse matrix of the Hamiltonian with 128-bit complex numbers requires at least 100 PB, while

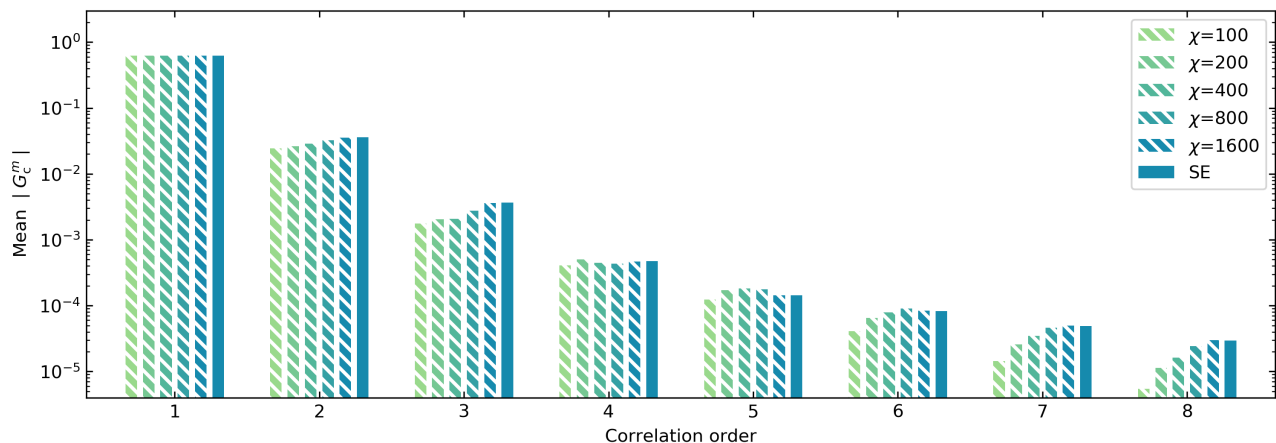


FIG. S9. **Comparison of numerics.** When increasing the bond dimension χ of the TDVP simulation, the correlation functions approach the values predicted by SE. These calculations are performed for the $L = 16$ and $N_b = 10$ system. The bond dimension of 1,600 approaches the maximum value of the bond during the evolution.

storing the dense matrix of the Hamiltonian requires 10^{13} PB memory. Both of them exceed the storage capability of 9.2 PB RAM on the *Frontier*.

5.2. Time-dependent variational principle

For large systems, the memory is insufficient in the *Hanhai20* clusters to perform the exact simulation. Thus we exploit the TDVP [60] to simulate the dynamics, which is memory-efficient and is capable of performing the simulation up to 32 sites. The simulation is implemented based on the package *TeNPy* [61]. The time cost of the simulation shows an exponential scaling versus the bond dimension. We fix the bond dimension to 200 for the self-consistent iteration of the local energy offsets mentioned in Section 2.3, which perfectly approximates the results from SE in terms of the density profile. In all classical simulations, we restrict the state per site (sps) to be 5.

5.3. Comparison of the numerics

The prediction of the multi-point correlation functions for the (32,16) system reported in Fig. 4 is from a TDVP simulation. We found that the predicted values are underestimated compared with the experimental data, especially in higher-order correlations. This is attributed to the cut-off of the bond dimension, which leads to an MPS involving less entanglement. To examine the guess, we vary the bond dimension from 100 to 1,600 for the simulations in the (16,10) system. As shown in Fig. S9, for smaller bond dimensions, the lower-order correlations are consistent with those from SE, while the higher-order correlations are weaker than those from SE. Until the bond dimension increases to the upper limit, i.e., there

is no cut-off during the evolution, the eighth-order correlation approaches the value predicted by SE. For larger systems and higher-order correlations, the required bond dimension of the TDVP simulation to reproduce the experimental results will increase as well, which is infeasible even with the TDVP method.

6. DATA ANALYSIS

6.1. Sample collection

The average filling of the initial state is about 96%. Besides, some of the atoms will hop outside the chain during the driving dynamics or expanding for detection. Thus, the realizations in which there are atoms outside the chain are rejected. We also post-select the samples that the total number of the detected atoms in the L -site chain is exact N_b and the atom number in each site is less than 5. Similarly, in the entanglement entropy measurements, we post-select the realizations where the total parity in the 2×6 -site plaquette is even. For the largest system of 32 sites and 20 atoms, we typically retain 8% of the data, corresponding to a sampling rate of one sample every 500 seconds.

6.2. Mock-up distributions

We propose six competitive mock-up distributions in the Bayesian tests. The Initial mock-up is that the probability of the string corresponding to the initial state is unity, and is zero otherwise.

$$p_{\text{init}}(z_i) = \begin{cases} 1, & z_i = 01 \cdots 10, \\ 0, & \text{otherwise,} \end{cases} \quad (\text{S4})$$

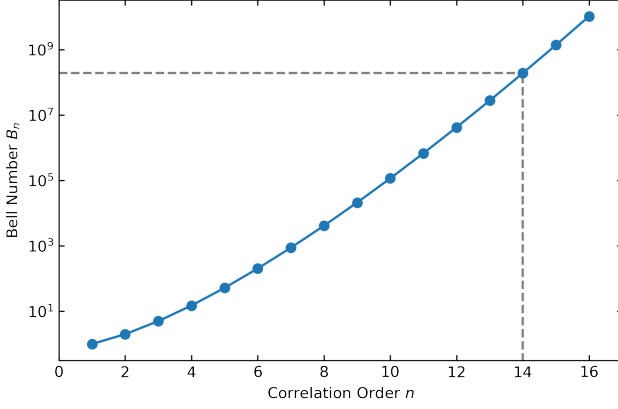


FIG. S10. **Bell Numbers.** The number of terms in multi-point density correlation functions shows an explosive growth trend as the order increases. The highest order we calculated for $L = 32, N_b = 20$ is 14th, which contains about 10^8 lower order terms.

The second mock-up is the Uniform distribution, which is a flat distribution over the whole strings.

$$p_{\text{uni}}(z_i) = \frac{1}{N_s}, \quad (\text{S5})$$

where N_s is the dimension of the Hilbert space. The

other mock-ups are derived from the NSBHM, which share identical Hubbard parameters except one of them with the ideal probability distribution. For instance, the Disorderless mock-up is calculated based on a NSBHM without disorder potential, and the Undriven one is derived from that without the driving term. For the MBL and GOE mock-up, we choose an amplitude of $20 \times W$ for the disorder potential and an driving frequency of $20 \times \omega$ for the simulations, respectively. All the calculations are based on SE.

6.3. Multi-point correlation functions

The joint expectation value of operators $\{\hat{n}_i\}$ is $\langle \prod_{i=1}^m \hat{n}_i \rangle = \langle \hat{n}_1 \hat{n}_2 \dots \hat{n}_m \rangle$, captures two kinds of correlations: “disconnected” correlations and “connected” correlations. The multi-point density correlation function measured in our experiment is the “connected” part. It includes only the m -th order correlations and cannot be described by lower-order correlations.

In the main text, Eq. 3 gives the recursive formula of the multi-point density correlation function. Here, we write down a four-point case (Eq. S6) explicitly as an example:

$$\begin{aligned}
G_c^4(x_1, x_2, x_3, x_4) &= G_{\text{tot}}^4(x_1, x_2, x_3, x_4) - G_{\text{dis}}^4(x_1, x_2, x_3, x_4) \\
&= \langle \hat{n}_1 \hat{n}_2 \hat{n}_3 \hat{n}_4 \rangle - \left[G_c^3(x_1, x_2, x_3) \langle \hat{n}_4 \rangle + G_c^3(x_1, x_2, x_4) \langle \hat{n}_3 \rangle + G_c^3(x_1, x_3, x_4) \langle \hat{n}_2 \rangle + G_c^3(x_2, x_3, x_4) \langle \hat{n}_1 \rangle \right] \\
&\quad - \left[G_c^2(x_1, x_2) G_c^2(x_3, x_4) + G_c^2(x_1, x_3) G_c^2(x_2, x_4) + G_c^2(x_1, x_4) G_c^2(x_2, x_3) \right] \\
&\quad - \left[G_c^2(x_1, x_2) \langle \hat{n}_3 \rangle \langle \hat{n}_4 \rangle + G_c^2(x_1, x_3) \langle \hat{n}_2 \rangle \langle \hat{n}_4 \rangle + G_c^2(x_1, x_4) \langle \hat{n}_2 \rangle \langle \hat{n}_3 \rangle + G_c^2(x_2, x_3) \langle \hat{n}_1 \rangle \langle \hat{n}_4 \rangle \right. \\
&\quad \left. + G_c^2(x_2, x_4) \langle \hat{n}_1 \rangle \langle \hat{n}_3 \rangle + G_c^2(x_3, x_4) \langle \hat{n}_1 \rangle \langle \hat{n}_2 \rangle \right] - \langle \hat{n}_1 \rangle \langle \hat{n}_2 \rangle \langle \hat{n}_3 \rangle \langle \hat{n}_4 \rangle
\end{aligned} \quad (\text{S6})$$

We find that the “disconnected” part consists of the integer partitions of the involved lattice sites with at least two nonzero integers. For the three-point case, the groupings are $\{(2, 1), (1, 1, 1)\}$, where $(2, 1)$ contains three cases: $(x_1, x_2; x_3)$, $(x_1, x_3; x_2)$ and $(x_2, x_3; x_1)$. Hence, G_{dis}^3 has four terms in total. For the four-point case, as mentioned above, we can divide them into $\{(3, 1), (2, 2), (2, 1, 1), (1, 1, 1, 1)\}$, and the number of cases for each partition is $\{4, 3, 6, 1\}$, leading to a total amount of fourteen terms in G_{dis}^4 .

The number of terms in the “connected” correlation (G_{tot}^m is also included here), is called the Bell numbers, corresponding to a partitioning problem. In Ref. [54], E.T. Bell gave the definition of Bell numbers: The Bell number B_n is the number of ways to divide a set with

n elements into disjoint, nonempty subsets. $B_0 = 1$ because there is only one partition of an empty set. Eq. S7 reveals the recursive relationship of the Bell numbers in terms of binomial coefficients (Ref. [56]).

$$B_{n+1} = \sum_{k=0}^n C_n^k B_k \quad (\text{S7})$$

Therefore, as the order of the correlation increases, the number of terms in multi-point density correlation functions will have an explosive growth trend, which is shown in Fig. S10. The 14th-order correlation contains about 10^8 lower-order terms. Besides, to obtain the mean value of $|G_c^{14}(\mathbf{x})|$, there are C_{32}^{14} configurations of subsystems involving 14 sites in the 32-site chain. Hence, in the

system of (32,20), we select only 100 configurations randomly to average.

-
- [46] Xiao, B. *et al.* Generating two-dimensional quantum gases with high stability. *Chinese Phys. B* **29**, 076701 (2020).
- [47] Yang, B. *et al.* Spin-dependent optical superlattice. *Phys. Rev. A* **96**, 011602 (2017).
- [48] Zheng, Y.-G. *et al.* A compact gain-enhanced microwave helical antenna for 87 Rb atomic experiments. *Rev. Sci. Instrum.* **93**, 064701 (2022).
- [49] Zheng, Y.-G. *et al.* Robust site-resolved addressing via dynamically tracking the phase of optical lattices. *Opt. Lett.* **47**, 4239 (2022).
- [50] DePue, M. T., McCormick, C., Winoto, S. L., Oliver, S. & Weiss, D. S. Unity occupation of sites in a 3D optical lattice. *Phys. Rev. Lett.* **82**, 2262–2265 (1999).
- [51] Daley, A. J., Pichler, H., Schachenmayer, J. & Zoller, P. Measuring entanglement growth in quench dynamics of bosons in an optical lattice. *Phys. Rev. Lett.* **109**, 020205 (2012).
- [52] Bluvstein, D. *et al.* A quantum processor based on coherent transport of entangled atom arrays. *Nature* **604**, 451–456 (2022).
- [53] Lukin, A. *et al.* Probing entanglement in a many-body-localized system. *Science* **364**, 256–260 (2019).
- [54] Bell, E. T. Exponential numbers. *Am. Math. Mon.* **41**, 411–419 (1934).
- [55] Stringari, S. Collective excitations of a trapped Bose-condensed gas. *Phys. Rev. Lett.* **77**, 2360 (1996).
- [56] Wilf, H. S. *generatingfunctionology* (CRC press, 2005).
- [57] Weinberg, P. & Bukov, M. Quspin: a python package for dynamics and exact diagonalisation of quantum many body systems. part ii: bosons, fermions and higher spins. *SciPost Phys.* **7**, 020 (2019).
- [58] Virtanen, P. *et al.* SciPy 1.0: Fundamental Algorithms for Scientific Computing in Python. *Nat. Method* **17**, 261–272 (2020).
- [59] Dahlgren, B. pyodesys: Straightforward numerical integration of ODE systems from Python. *J. Open Sour. Soft.* **3**, 490 (2018).
- [60] Haegeman, J., Lubich, C., Oseledets, I., Vandereycken, B. & Verstraete, F. Unifying time evolution and optimization with matrix product states. *Phys. Rev. B* **94**, 165116 (2016).
- [61] Hauschild, J. & Pollmann, F. Efficient numerical simulations with tensor networks: Tensor network python (tenpy). *SciPost Phys. Lect. Notes* 005 (2018).